nature geoscience

Article

https://doi.org/10.1038/s41561-025-01875-1

Canadian net forest CO_2 uptake enhanced by heat drought via reduced respiration

Received: 28 April 2025

Accepted: 5 November 2025

Guanyu Dong[1], **Fei Jiang**[1,2,3] ✉, **Yongguang Zhang**[1,2,3], **Weimin Ju**[1], **Shilong Piao**[4], **Philippe Ciais**[5], **Wouter Peters**[6], **Ingrid T. Luijkx**[6], **Junjie Liu**[7], **Frédéric Chevallier**[5], **Ning Zeng**[8], **Xiangjun Tian**[9], **Shamil Maksyutov**[10], **Oliver Sonnentag**[11], **M. Altaf Arain**[12], **Alan G. Barr**[13], **Yuanyuan Huang**[14], **Chao Yue**[15], **Wenping Yuan**[4], **Liangyun Liu**[16], **Lei Fan**[17], **Xu Yue**[18], **Jingfeng Xiao**[19], **Xing Li**[20], **Stephen Sitch**[21], **Pierre Friedlingstein**[21,22], **Michael O'Sullivan**[21], **Jürgen Knauer**[23,24], **Vivek Arora**[25], **Daniel Kennedy**[26], **Lei Ma**[27], **Peter E. Thornton**[28], **Roland Séférian**[29], **Tobias Nützel**[30], **Jens Heinke**[31], **Qing Sun**[32,33,34], **Sönke Zaehle**[35], **Philippe Peylin**[5], **Etsushi Kato**[36], **Haley Alcock**[11], **Bruno Lecavalier**[11], **Mousong Wu**[1], **Jun Wang**[1], **Lingyu Zhang**[1], **Guoyuan Lv**[1], **Yuanyuan Zhang**[1], **Dayang Zhao**[1] & **Jing M. Chen**[37,38]

The response of net forest carbon uptake to warm extremes remains elusive. The year 2023 was at the time 'the hottest year on record' globally, with Canada's forests experiencing warm anomalies of above 2 °C and unprecedented drought and wildfires, providing a unique case to examine the response of boreal forest net carbon uptake to climate extremes. Here we combine satellite-based atmospheric CO_2 flux inversions with ground-based in situ observations of CO_2 fluxes and concentrations to investigate Canada's forest net carbon uptake and its underlying mechanisms in 2023. We find that, compared with 2015–2022, Canada's forest net carbon uptake was enhanced by 0.28 ± 0.23 PgC, offsetting 38–48% of Canadian wildfire emissions in 2023. This enhanced net uptake was dominated by large ecosystem respiration reductions, mainly attributable to severe root-zone soil moisture deficits and the unimodal temperature response of respiration. However, most dynamic global vegetation models failed to simulate the respiration reductions and the responses to hydrothermal conditions well. This study improves our understanding of boreal forest net carbon uptake in response to climate extremes and highlights an urgent need to improve vegetation models under global warming.

Terrestrial ecosystems absorb ~30% of anthropogenic carbon dioxide (CO_2) emissions, playing a critical role in mitigating climate change[1]. However, it is threatened by disturbances such as weather extremes[2], which may lead to carbon losses through reduced gross primary production (GPP) and/or increased total ecosystem respiration (TER) and disturbance[3]. Interannual variability (IAV) of global net land CO_2 flux (net biome production; NBP) is typically caused more by the variations in GPP rather than TER[4], but large uncertainties remain in their relative contributions at regional scales[4]. Earth system model projections of land sink trends over the twenty-first century under future warming remain highly uncertain, varying widely from positive to negative[5,6]. These uncertainties largely stem from incomplete understanding of terrestrial carbon cycle processes.

Boreal forests play an important role in the terrestrial carbon cycle on Earth[7,8], holding about 30% of the global forest carbon stocks[9]. Canada's forests, covering one-third of the boreal forests[10], absorb a

A full list of affiliations appears at the end of the paper. ✉e-mail: jiangf@nju.edu.cn

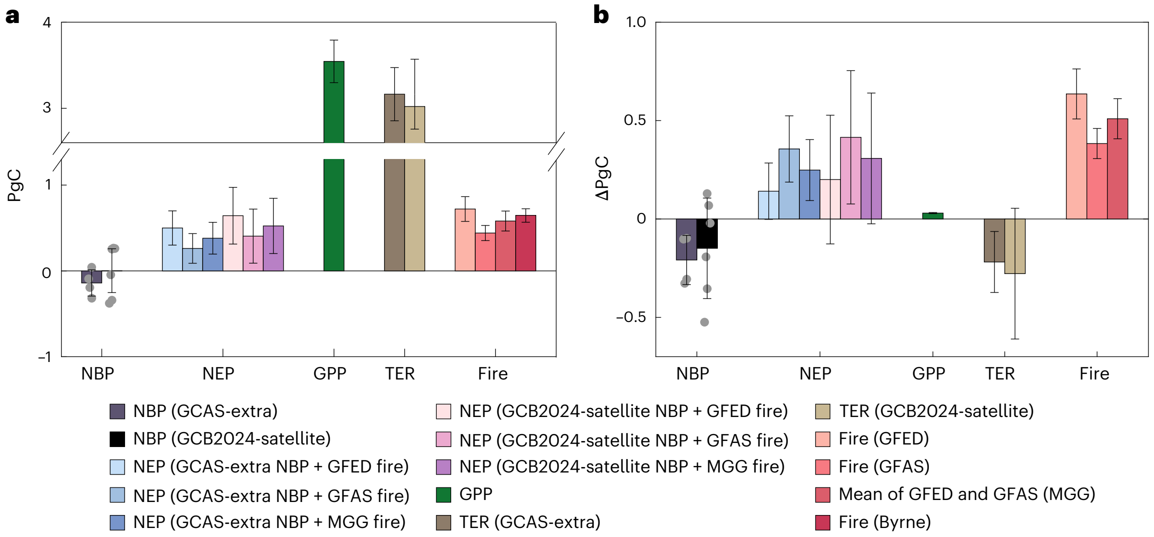

Fig. 1 | Terrestrial carbon fluxes in 2023 and their anomalies relative to 2015–2022 over the Canadian forests. a,**b**, Terrestrial carbon fluxes (that is, NBP, NEP, GPP, TER and wildfire emissions) in 2023 (**a**) and their anomalies relative to 2015–2022 (**b**). NBP is from GCAS-extra and GCB2024-satellite inversions; NEP is estimated as the sum of NBP and wildfire emissions (including GFED4.1s, GFAS, mean of GFED and GFAS (MGG)). GPP is the mean of GOSIF GPP and FluxSat GPP. TER in **a** and **b** is separated from NBP by using MGG wildfire emissions and GPP. Bars represent optimal estimates of these carbon fluxes, and error bars represent uncertainties of these carbon fluxes. For the uncertainties, NBP is calculated as the standard deviation of ensembles ($n = 4$ for GCAS-extra inversion ensembles, $n = 6$ for GCB2024-satellite inversion ensembles), wildfire emissions are assumed to be 20%, GPP is estimated using the standard deviation of the bootstrapped GPP ensembles ($n = 1{,}000$) and NEP and TER are estimated using equations (3) and (5), respectively.

large amount of CO_2 every year and are considered important in mitigating the increasing growth rate of atmospheric CO_2 concentrations and climatic warming[9,10]. However, although Canada's forest carbon uptake may benefit from warming by increasing production[11,12], carbon losses associated with wildfires and weather extremes can offset the enhanced uptake and even turn it from a sink into a source[13]. Recent studies based on eddy covariance (EC) and chamber measurements have provided insights into drought effects on boreal forest carbon uptake[14,15], but the contributions of GPP and TER to changes in net forest uptake remain controversial. Also, the mechanisms regarding the boreal forest drought response at regional scale are still poorly understood. The year 2023 was at that time the hottest year globally on record since 1850[16], with Canada experiencing extreme high temperature and drought (Supplementary Fig. 1). Widespread air temperature anomalies exceeding 2 °C were observed in Canada, concurrent with unprecedented low precipitation (Supplementary Fig. 1a), leading to severe drought and wildfires[17]. This situation provides a unique case to investigate the impact of heat drought on the boreal forest net carbon uptake (we use 'heat drought' to refer to a compound event of high temperatures and persistent dryness).

Atmospheric inversions use atmospheric transport models combined with atmospheric CO_2 observations to quantify global and/or regional terrestrial carbon sinks or sources[18,19]. Compared with surface CO_2 measurements, satellite column-averaged dry air CO_2 mole fraction (XCO_2) observations have better spatial coverage and can therefore improve the estimates of NBP and its responses to climate extremes[20]. By assimilating satellite XCO_2 observations, atmospheric inversions have been widely used to study the responses of terrestrial ecosystem carbon sinks to climate extremes such as the 2015/2016 El Niño, the 2021 La Niña, the 2019 Indian Ocean Dipole and regional droughts in China and North America[3,21–23].

Here, we investigate the responses of Canada's net forest carbon uptake (that is, NEP = NBP + wildfires) to climate extremes using an ensemble of NBP from the Global Carbon Budget 2024 (GCB2024) atmospheric inversions[1]. Due to fewer in situ CO_2 observations in Canada in 2023 than in previous years, this study primarily uses satellite-constrained NBP (hereafter GCB2024-satellite), supplemented by in-situ-constrained estimates (hereafter GCB2024-in-situ). Considering the influence of prior fluxes IAV on inverted NBP IAV, we perform extra inversions using the Global Carbon Assimilation System[24], version 2 (hereafter GCAS-extra; Methods). Two wildfire emission datasets were used to reduce the uncertainty in NEP estimates, and two satellite-derived GPP products were then utilized to separate TER (TER = GPP − NEP). We also analyse in situ observations of CO_2 fluxes and concentrations, as well as simulations of dynamic global vegetation models (DGVMs) from the TRENDYv13 project[1,25]. We aim to address the following key questions: (1) How does the NEP of Canada's forests change in 2023 compared with 2015–2022? (2) Which carbon cycle process is primarily responsible for this change?

Enhanced net carbon uptake of Canada's forests in 2023

Our estimates of the annual NBP in 2023 from GCB2024-satellite and GCAS-extra inversions are 0.003 ± 0.30 PgC yr^{-1} and −0.14 ± 0.15 PgC yr^{-1} (sink positive/source negative, same thereafter) (Fig. 1a), and all show negative anomalies for 2023 relative to 2015–2022. Surprisingly, when using different wildfire emissions (that is, Global Fire Emissions Databases v4.1 (GFED4.1s), Global Fire Assimilation System (GFAS) and mean of GFED4.1s and GFAS (MGG)) to separate NEP from atmospheric inversion-derived NBP, we find overall positive NEP anomalies (Fig. 1b), despite extreme heat drought and unprecedented wildfires occurring in 2023. Because uncertainty in wildfire emissions can be passed into the NEP estimates, we compare the GFED4.1s, GFAS and MGG emissions with a recent top-down estimate for the 2023 Canadian wildfire emissions[26] (hereafter Byrne emissions) and find that MGG emissions are closest to the Byrne emissions (Fig. 1a). Thus, we use MGG as the optimal estimate for wildfire emissions to provide the optimal NEP estimates. Moreover, to fully remove the effect of wildfire emissions on NEP estimates, we calculate NEP scenarios for regions with no or only little wildfires occurrence, which show similar NEP anomalies (Supplementary Fig. 2), indicating that the estimated NEP anomalies for 2023 are robust. We estimate the NEP anomalies for 2023 are 0.31 ± 0.33 PgC yr^{-1} and 0.25 ± 0.15 PgC yr^{-1} based on the GCB2024-satellite and GCAS-extra inversions, respectively. Similar results are also found based on the

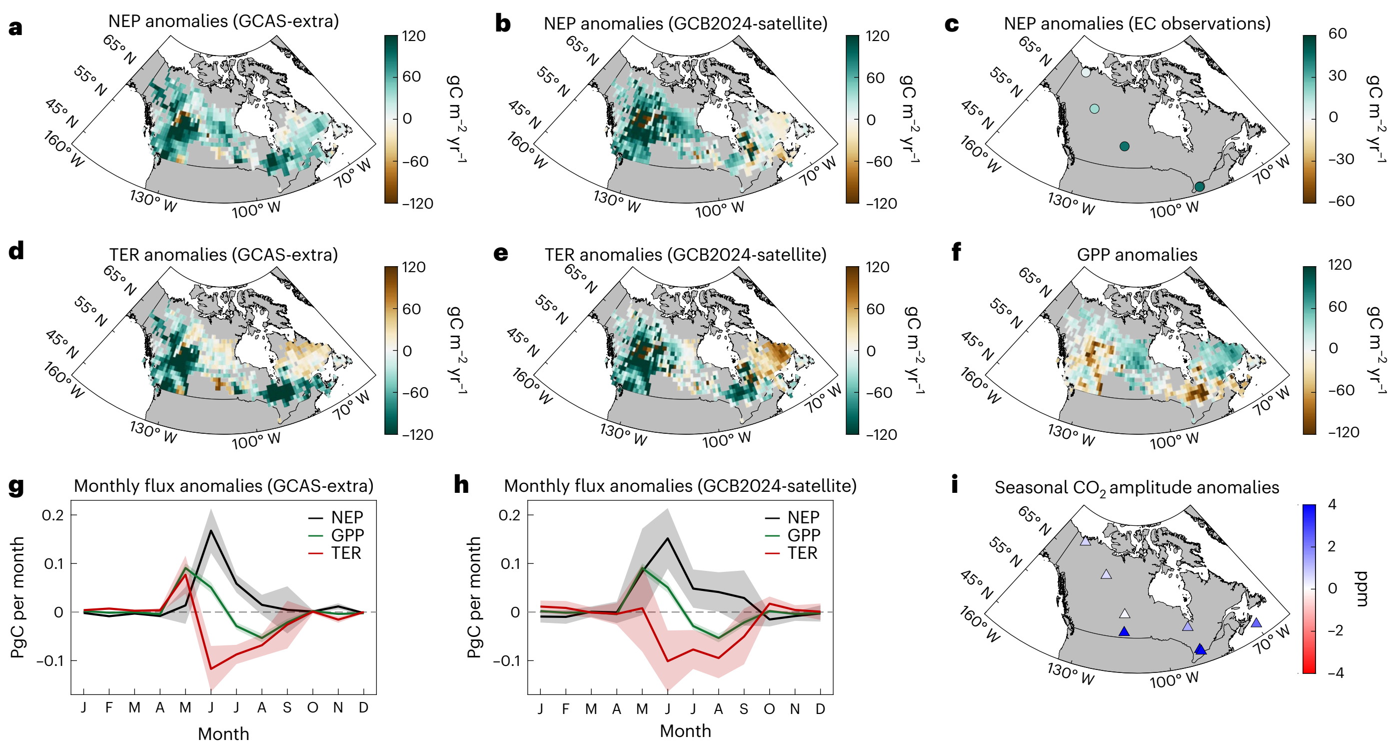

Fig. 2 | The NEP, GPP and TER anomalies over Canada's forests in 2023, relative to the 2015–2022 average. **a**,**b**, The spatial distribution of annual mean NEP anomalies in 2023 calculated on the basis of GCAS-extra (**a**) and GCB2024-satellite (**b**) inversions, respectively. **c**, NEP anomalies in 2023 for each EC site. **d**,**e**, The spatial distribution of annual mean TER anomalies in 2023 constructed from GCAS-extra (**d**) and GCB2024-satellite (**e**) inversions, wildfire emissions and independent GPP products. **f**, The spatial distribution of annual mean GPP anomalies in 2023. **g**,**h**, Monthly anomalies of the NEP, GPP and TER in 2023 over Canada's forests based on GCAS-extra (**g**) and GCB2024-satellite (**h**) inversions. **i**, SA anomalies of CO_2 concentrations in 2023 for each surface station. Lines in **g** and **h** represent optimal estimates of NEP, GPP and TER, and shaded areas represent the uncertainties of NEP, GPP and TER. The uncertainty of GPP is estimated using the standard deviation of the bootstrapped GPP ensembles ($n = 1{,}000$), and those of NEP and TER are estimated using equations (3) and (5), respectively. Basemap data in **a**–**f**,**i** from Esri, Garmin International, Inc., US Central Intelligence Agency and National Geographic Society.

GCB2024-in-situ inversions (Supplementary Fig. 3). These suggest an enhanced net ecosystem CO_2 uptake by Canada's forests in the extremely hot and dry year 2023.

The 2023 NEP in Canadian forests ranked as the largest during 2015–2023. Compared with 2015–2022, widespread positive NEP anomalies in 2023 were observed, mainly in western and parts of southeastern Canada (Fig. 2a,b). The positive NEP anomalies started in May and peaked in June, then returned close to zero in October (Fig. 2g,h), namely most positive NEP anomalies occurred in summer (June–August; Supplementary Fig. 4). We also quantify seasonal NEP anomalies across dominant plant functional types (PFTs), that is, conifer forest, mixed forest and northern taiga (Supplementary Fig. 5). All three dominant PFTs show similar patterns of seasonal NEP anomalies, with conifer forests dominating the NEP anomalies (Supplementary Fig. 6). Furthermore, the in situ flux observations from five sites show pronounced positive NEP anomalies as well (Fig. 2c and Supplementary Fig. 7). The IAV of atmospheric CO_2 seasonal amplitudes (SAs) can reflect the NEP changes in a region to some extent[4,27]. We calculate the SAs during 2015–2023 using the OCO-2 XCO_2 retrievals and atmospheric CO_2 concentrations from eight sites in Canada (Methods). The results show that satellite XCO_2 SAs are the largest in 2023 and most surface stations exhibit obvious positive SA anomalies for 2023 relative to 2015–2022 (Fig. 2i, Supplementary Fig. 8 and Supplementary Table 1). Overall, these results all suggest an enhanced NEP in Canadian forests in 2023.

Large reductions in respiration dominate the enhanced uptake

We further analyse the two components of NEP: GPP and TER. Compared with 2015–2022, overall negative TER anomalies were observed in 2023 (-0.28 ± 0.33 PgC yr^{-1} and -0.22 ± 0.16 PgC yr^{-1} based on GCB2024-satellite and GCAS-extra inversions, respectively; Fig. 1b). Areas with substantial TER reductions show notable positive NEP anomalies (Fig. 2), confirmed by flux observations at the Scotty Creek Landscape (CA-SCC) site located near the enhanced NEP hotspot regions in northwestern Canada (Supplementary Fig. 7). However, compared with TER anomalies, GPP increased marginally, despite reductions occurring in some regions with reduced respiration (Fig. 2f). These findings suggest that large reductions in TER, rather than increases in GPP, contributed to the enhanced forest NEP in Canada in 2023.

The mechanisms behind positive NEP anomalies varied monthly, owing to different responses of GPP and TER to 2023 climate anomalies. Minor NEP increases in May probably resulted from an earlier onset of growing season due to the higher spring temperatures (March–May)[28]. Warmer spring and the accompanying accelerated snowmelt enhanced photosynthesis[29] (Supplementary Fig. 9), as indicated by a strong positive correlation ($r = 0.63$, $P < 0.01$) between May GPP anomalies and spring temperature anomalies (Supplementary Fig. 10b). However, due to the concurrent stimulation of TER by a warmer spring, most GPP increases were offset by TER increases, resulting in small positive NEP anomalies in May.

The positive GPP anomalies in June were probably attributable to warmer spring effects on early-summer forest productivity[30–32]. In contrast to the increased GPP, TER showed striking reductions and thus dominated the positive NEP anomalies in June (Fig. 2g,h and Supplementary Figs. 11 and 12). Due to the persistent root-zone soil moisture (RZSM) deficit and high temperature (Supplementary Fig. 9), the GPP anomalies shifted from positive to negative in July, while negative TER anomalies remained. As TER

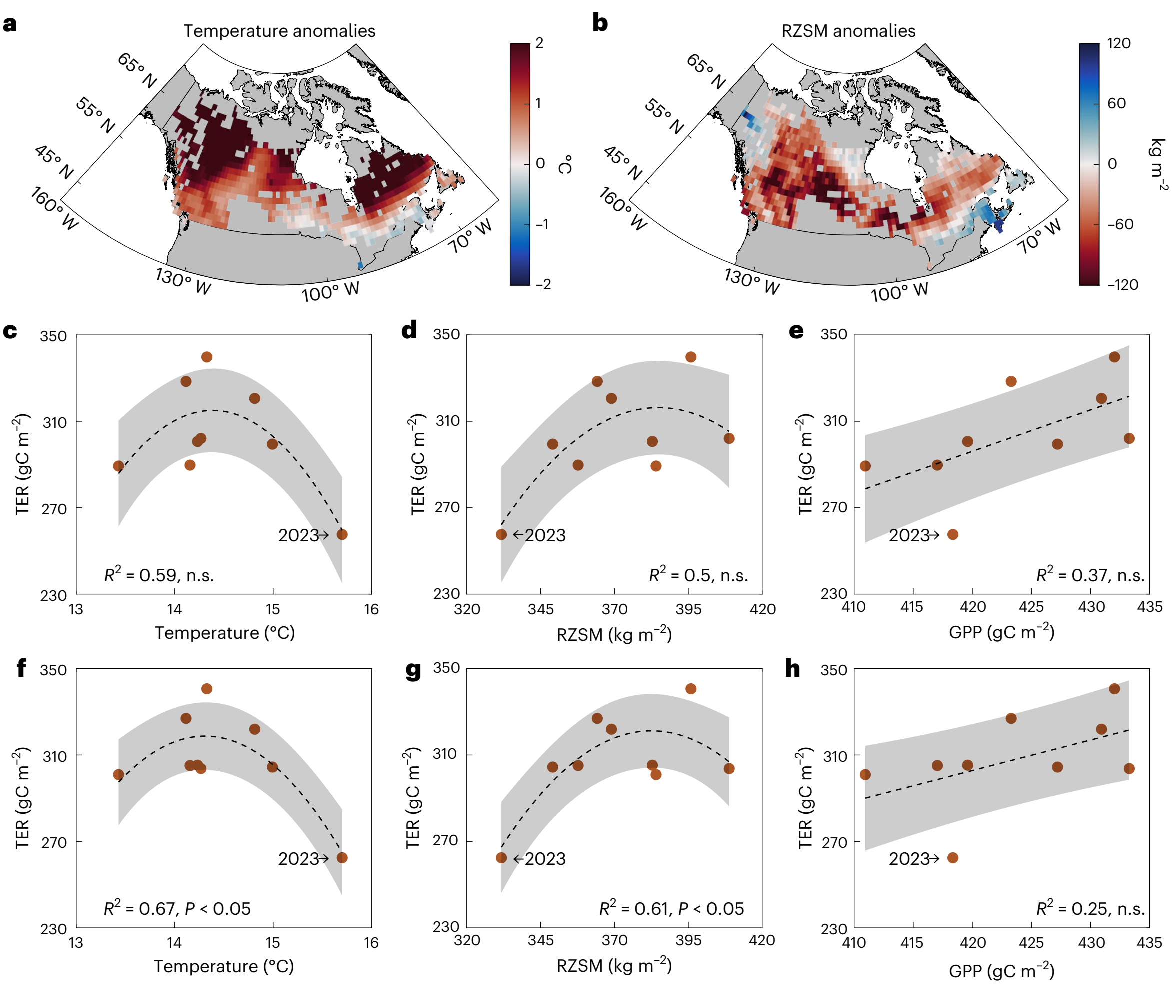

Fig. 3 | Responses of TER to GPP, air temperature and RZSM during summer (June–August) 2015–2023 over Canadian forests. a,**b**, Spatial patterns of the RZSM (**a**) and air temperature (**b**) anomalies in summer 2023, relative to the 2015–2022 summer average. **c**–**e**, The relationship between the TER and air temperature (**c**), RZSM (**d**) and GPP (**e**) in summer. TER in **c**–**e** is constructed from GCAS-extra inversions, wildfire emissions and independent GPP products. **f**–**h**, The same as **c** (**f**), **d** (**g**) and **e** (**h**), but TER is constructed from GCB2024-satellite inversions. The TER–RZSM and TER–temperature response curves were fitted by a second-order polynomial model, and the TER–GPP response curve was fitted by a linear model (Methods). The red points in **c**–**h** represent the total value of summer TER. The dashed lines represent the regression lines fitted to the data, while the shaded areas represent the 95% confidence interval. GPP is the mean of GOSIF GPP and FluxSat GPP. Air temperature and RZSM are taken from ERA5-Land and GLDAS, respectively. Statistical significance of the model fitting was calculated using the *F*-test. 'n.s.' indicates no statistically significant relationship when $P > 0.05$. Basemap data in **a** and **b** from Esri, Garmin International, Inc., US Central Intelligence Agency and National Geographic Society.

reductions were greater than GPP reductions, positive NEP anomalies persisted until mid-autumn (Fig. 2g,h).

Subsequent decreases in GPP could be explained by reduced stomatal conductance, which is associated with enhanced water use efficiency and reduced evaporative losses at the expense of vegetation photosynthesis during the summer drought conditions[33]. This can be confirmed by the reductions in canopy near-infrared reflectance detected by recently proposed kernel normalize difference vegetation index (kNDVI) and solar-induced chlorophyll fluorescence (SIF). The spatial–temporal patterns of summer kNDVI and SIF anomalies agree well with those of summer GPP anomalies (Supplementary Fig. 4), independently supporting reduced GPP during the summer drought.

However, the TRENDYv13 DGVMs show large divergences in simulating Canada's NEP over the study period (Supplementary Figs. 13–16). Only about half of the DGVMs show increased uptake in 2023, largely due to increased GPP rather than reduced TER (Supplementary Figs. 17–21). The IAVs of NEP and TER show a weak correlation between our atmospheric inversion-based estimates and the ensemble mean of the 14 TRENDY DGVMs ($r = 0.38$, $P > 0.05$ for NEP; $r = 0.12$, $P > 0.05$ for TER) (Supplementary Table 2). By contrast, the DGVM-simulated and satellite-derived GPP IAVs show a strong correlation ($r = 0.81$, $P < 0.01$). Thus, the large discrepancy in quantifying the 2023 Canada's NEP between DGVM simulations and atmospheric inversion-based estimates may arise from the inability of DGVMs to accurately simulate TER dynamics.

Attribution of the reduced respiration

During the summer 2023, most Canadian forests experienced high temperature anomalies above 2 °C relative to 2015–2022, alongside severe drought (Fig. 3a,b). This drought progression stemmed primarily from persistent precipitation deficits since August 2022 and extremely high spring-summer temperatures in 2023 (Supplementary Fig. 9). Besides, the earlier onset of vegetation phenology in 2023 could further reduce late-spring soil moisture through increased evapotranspiration, exacerbating the 2023 summer drought[34]. The 2023 summer TER reached its lowest level in the past 9 years, associated with the hot and dry conditions and GPP reductions induced by drought (Fig. 3c–h). We thus fit the relationships between TER and temperature, RZSM and satellite-derived GPP during summer 2015–2023 (Methods). The relationship between TER and temperature is a unimodal shape: TER rises

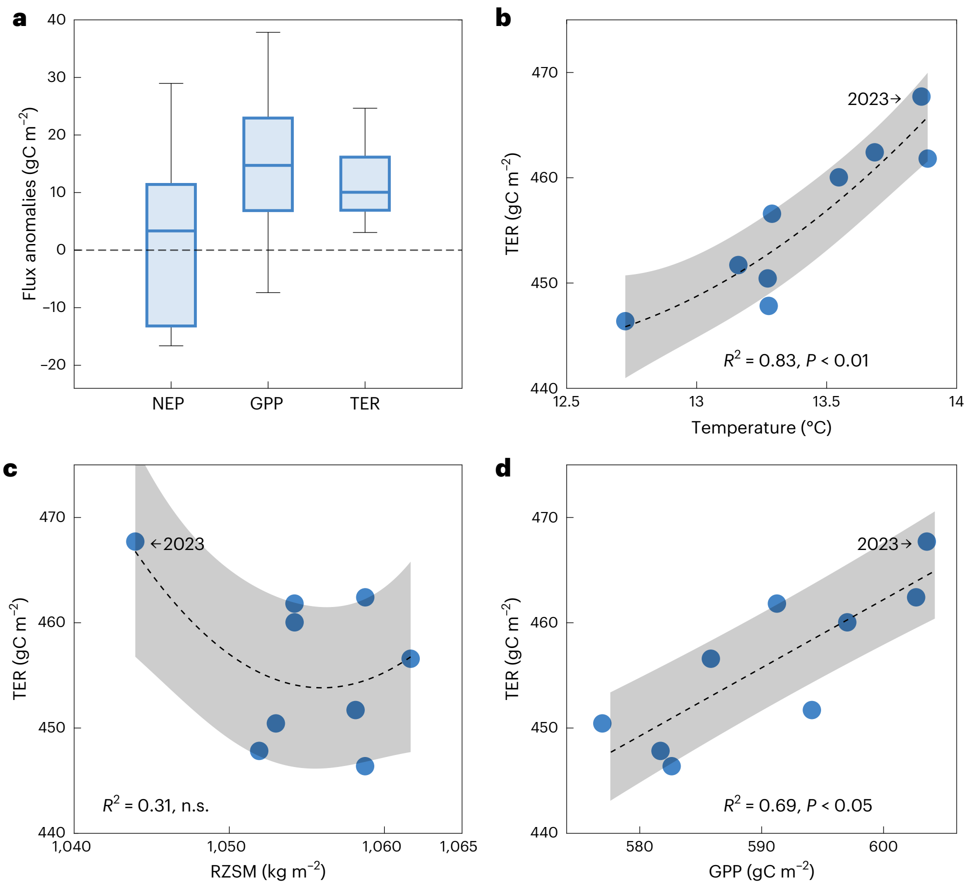

Fig. 4 | Relationships between TER and air temperature, RZSM and GPP in summer 2015–2023, estimated using the ensemble mean of 14 TRENDYv13 DGVMs. a, Anomalies of NEP, GPP and TER for summer 2023 relative to 2015–2022 (n = 14). Data are presented as box plots showing the median (centre line), the 25th and 75th percentiles (box limits) and the whiskers extending to the minimum and maximum data points. **b**–**d**, Relationships between the TER and air temperature (**b**), RZSM (**c**) and GPP (**d**) in summer. The TER–RZSM and TER–temperature response curves were fitted by a second-order polynomial model, and the TER–GPP response curve was fitted by a linear model. The dashed lines represent the regression lines fitted to the data, and the shaded areas represent the 95% confidence interval. TER, air temperature, RZSM and GPP are taken by the TRENDYv13 DGVMs. Statistical significance of the model fitting was calculated using the F-test. 'n.s.' indicates no statistically significant relationship when $P > 0.05$.

to a maximum value at an optimal temperature (T_{opt}) and then declines as temperature increases further (Fig. 3c,f and Supplementary Figs. 22 and 23). This summer T_{opt} (14–15 °C) is close to the apparent T_{opt} of 16 °C observed at the CA-SCC site (Supplementary Fig. 24) and a previous EC site-based study[35] in Canada's forests.

Similar to the TER–temperature response curve, TER increases with RZSM and peaks at specific RZSM as well (Fig. 3d,g). The TER reductions occur when RZSM is in deficit or exceeds a threshold of ~380 kg m^{-2}, indicating the effect of moisture, oxygen and substrate limitations on the metabolism of TER[36]. Given uncertainties in the RZSM product, we test an alternative soil moisture dataset and find consistent TER–RZSM relationships (Supplementary Fig. 25). Severe RZSM deficits are accompanied by extreme high temperatures, which could exacerbate TER reductions. In addition, vegetation photosynthesis can directly affect autotrophic respiration and indirectly affect heterotrophic respiration via altered carbon inputs to soil[37,38], which could be reflected in the linear relationship between GPP and TER (Fig. 3e,h). The relationships between TER and both hydrothermal conditions and GPP are similar across the dominant PFTs, but the T_{opt} and RZSM thresholds are different (Supplementary Figs. 26–28). Northern taiga shows a higher temperature sensitivity of TER than conifer forests and mixed forests, which is related to the local climate conditions for plant growth. Further analysis of these relationships across different climate zones reveals that the response of TER to hydrothermal conditions is also similar across different climate zones, and forested regions with cold summers tend to exhibit a higher temperature sensitivity of TER than those with warm summers (Supplementary Figs. 29–31). We further perform a statistical analysis to separate the contributions of GPP and environmental changes on the TER anomalies (Methods) and find that environmental factors (that is, air temperature and RZSM) are the primary drivers, explaining two-thirds of the total anomalies, whereas the influence of GPP is limited (Supplementary Fig. 32). Therefore, the 2023 summer TER reductions were mainly attributed to the severe RZSM deficits and supra-optimal temperatures over Canada's forests.

However, the summer TER–temperature relationship in DGVMs is quite different from our inversion-based results. DGVMs depict a monotonic TER increase with warming during 2015–2023 (Fig. 4b), whether it is a C or C–N coupling model (Supplementary Figs. 33 and 34). This failure to simulate the TER–temperature response may overestimate TER rates at higher temperatures[38]. In addition, while DGVMs reproduce the summer RZSM anomalies in 2023, some DGVMs are unable to capture the TER sensitivity to RZSM well (Fig. 4c and Supplementary Fig. 35). The DGVM-simulated linear TER–GPP relationship is identical to our inversion-based results, but most DGVMs do not show GPP reductions for 2023 summer drought, partially explaining the simulated TER increase in summer 2023 (Fig. 4d and Supplementary Fig. 36). Overall, these results have explained the TER increases in 2023 observed in DGVMs, as well as the discrepancy between the DGVM simulations and our atmospheric inversion-based results.

Implications of respiration reductions for carbon dynamics

We find an enhanced NEP of 0.28 ± 0.23 PgC for 2023 relative to 2015–2022 over the Canadian forests, which is equivalent to 148% of 2023 Canadian anthropogenic carbon emissions (694 Mt CO_2 equiv.)[39]. However, the Canadian wildfires in 2023 were unprecedented in both scale and intensity[17], with emissions reaching 0.65 (0.57–0.73) PgC (ref. 26). These findings suggest that climate extremes in 2023 in Canada not only triggered wildfires but also enhanced NEP by reduced forest respiration, thereby reducing the overall net carbon loss. We estimate that the enhanced forest NEP compensated for 38–48% of Canadian wildfire emissions in 2023.

The reasons for this enhanced NEP are twofold: (1) heat drought leads to large TER reductions, contributing ~90% of the NEP anomalies; and (2) the GPP increases in the warmer spring are offset by the reductions under summer drought, resulting in marginal annual GPP increases. This finding is consistent with previous observations at the Canadian Southern Old Aspen site during the 2001 drought[40,41] and at a mature temperate deciduous forest site within the Great Lakes region of Canada[42] during the 2012 heat drought. However, our results are in contrast to recent ground measurements in the 2018 summer drought in Europe[14,15], which suggest that the summer drought decreased boreal forest NEP by reducing understory production[14] and/or increasing heterotrophic respiration[15]. Such divergence may be due to the fact that the 2018 European summer drought was caused by extremely high positive anomalies in temperature and radiation rather than by moisture deficits, which is different from the climate anomalies observed in this study. The TER reductions under severe hot and dry conditions may be due to multiple mechanisms, such as reduced supply of photosynthetic substrates, suppressed root and soil microbial activities and respiratory enzyme capacity[43,44]. Meanwhile, RZSM deficits can inhibit the rhizosphere activity by reducing the transport of assimilates towards the rhizosphere[45].

Our results suggest that the TRENDY DGVM ensemble is unable to simulate the TER reductions in 2023 over Canada's forests. This may be due to incorrect TER–temperature and TER–RZSM responses in DGVMs or inappropriate settings of T_{opt}. Meanwhile, most DGVMs show GPP increases in summer 2023 relative to 2015–2022, which contradicts the reductions observed in satellite-derived GPP, potentially increasing the 2023 TER in DGVM simulations. Indeed, most DGVMs use Q_{10} or Arrhenius functions to represent exponential or near-exponential TER response to temperature[46,47]; only a limited number of models can simulate the unimodal temperature response of TER. In addition, TER simulated by DGVMs is overly sensitive to temperature but not sensitive enough to soil moisture[48]. These findings suggest that the responses of TER to hydrothermal conditions should be improved in DGVMs in the future.

In conclusion, this study challenges the conventional wisdom that extreme climate events reduce regional terrestrial carbon sinks. Previous studies suggested a weakening of boreal forest carbon sink under increasing and more severe heat-drought events[49,50]. In comparison, our results show that extreme heat drought in 2023 could counterintuitively increase boreal forest NEP by reducing TER, contradicting previous findings. Our findings imply that decreased TER can act as a partial buffer, offsetting carbon losses from increased mortality and reduced nutrient uptake under extreme heat-drought events. Therefore, accurate projections of the boreal forest carbon sink under global warming require realistic consideration of both GPP and TER dynamics.

Online content

Any methods, additional references, Nature Portfolio reporting summaries, source data, extended data, supplementary information, acknowledgements, peer review information; details of author contributions and competing interests; and statements of data and code availability are available at https://doi.org/10.1038/s41561-025-01875-1.

References

1. Friedlingstein, P. et al. Global Carbon Budget 2024. *Earth Syst. Sci. Data* **17**, 965–1039 (2025).
2. Reichstein, M. et al. Climate extremes and the carbon cycle. *Nature* **500**, 287–295 (2013).
3. Liu, J. et al. Contrasting carbon cycle responses of the tropical continents to the 2015–2016 El Niño. *Science* **358**, eaam5690 (2017).
4. Piao, S. L. et al. Interannual variation of terrestrial carbon cycle: Issues and perspectives. *Glob. Change Biol.* **26**, 300–318 (2020).
5. Luo, Y., Keenan, T. F. & Smith, M. Predictability of the terrestrial carbon cycle. *Glob. Change Biol.* **21**, 1737–1751 (2015).
6. Friedlingstein, P. et al. Uncertainties in CMIP5 climate projections due to carbon cycle feedbacks. *J. Clim.* **27**, 511–526 (2014).
7. Yang, H. et al. Global increase in biomass carbon stock dominated by growth of northern young forests over past decade. *Nat. Geosci.* **16**, 886–892 (2023).
8. Tagesson, T. et al. Recent divergence in the contributions of tropical and boreal forests to the terrestrial carbon sink. *Nat. Ecol. Evol.* **4**, 202–209 (2020).
9. Pan, Y. et al. The enduring world forest carbon sink. *Nature* **631**, 563–569 (2024).
10. Brandt, J. P., Flannigan, M. D., Maynard, D. G., Thompson, I. D. & Volney, W. J. A. An introduction to Canada's boreal zone: ecosystem processes, health, sustainability, and environmental issues. *Environ. Rev.* **21**, 207–226 (2013).
11. Wang, J., Taylor, A. R. & D'Orangeville, L. Warming-induced tree growth may help offset increasing disturbance across the Canadian boreal forest. *Proc. Natl Acad. Sci. USA* **120**, e2212780120 (2023).
12. D'Orangeville, L. et al. Northeastern North America as a potential refugium for boreal forests in a warming climate. *Science* **352**, 1452–1455 (2016).
13. Virkkala, A.-M. et al. Wildfires offset the increasing but spatially heterogeneous Arctic–boreal CO_2 uptake. *Nat. Clim. Change* **15**, 188–195 (2025).
14. Martínez-García, E. et al. Drought response of the boreal forest carbon sink is driven by understorey–tree composition. *Nat. Geosci.* **17**, 197–204 (2024).
15. Lindroth, A. et al. Effects of drought and meteorological forcing on carbon and water fluxes in Nordic forests during the dry summer of 2018. *Philos. Trans. R. Soc. B* **375**, 20190516 (2020).
16. Perkins-Kirkpatrick, S. et al. Extreme terrestrial heat in 2023. *Nat. Rev. Earth Environ.* **5**, 244–246 (2024).
17. Jain, P. et al. Drivers and impacts of the record-breaking 2023 wildfire season in Canada. *Nat. Commun.* **15**, 6764 (2024).
18. Peters, W. et al. An atmospheric perspective on North American carbon dioxide exchange: CarbonTracker. *Proc. Natl Acad. Sci. USA* **104**, 18925–18930 (2007).
19. Gurney, K. R. et al. Towards robust regional estimates of CO_2 sources and sinks using atmospheric transport models. *Nature* **415**, 626–630 (2002).
20. Chevallier, F. et al. Objective evaluation of surface- and satellite-driven carbon dioxide atmospheric inversions. *Atmos. Chem. Phys.* **19**, 14233–14251 (2019).
21. Liu, J. J. et al. Detecting drought impact on terrestrial biosphere carbon fluxes over contiguous US with satellite observations. *Environ. Res. Lett.* **13**, 095003 (2018).
22. Liu, J. et al. The reduced net carbon uptake over Northern Hemisphere land causes the close-to-normal CO_2 growth rate in 2021 La Nina. *Sci. Adv.* **10**, eadl2201 (2024).
23. Wang, J. et al. Enhanced India–Africa carbon uptake and Asia-Pacific carbon release associated with the 2019 extreme positive Indian Ocean dipole. *Geophys Res Lett.* **49**, e2022GL100950 (2022).

24. Jiang, F. et al. Regional CO_2 fluxes from 2010 to 2015 inferred from GOSAT XCO_2 retrievals using a new version of the Global Carbon Assimilation System. *Atmos. Chem. Phys.* **21**, 1963–1985 (2021).
25. Sitch, S. et al. Recent trends and drivers of regional sources and sinks of carbon dioxide. *Biogeosciences* **12**, 653–679 (2015).
26. Byrne, B. et al. Carbon emissions from the 2023 Canadian wildfires. *Nature* **633**, 835–839 (2024).
27. Liu, Z. et al. Seasonal CO_2 amplitude in northern high latitudes. *Nat. Rev. Earth Environ.* **5**, 802–817 (2024).
28. Wolf, S. et al. Warm spring reduced carbon cycle impact of the 2012 US summer drought. *Proc. Natl Acad. Sci.* **113**, 5880–5885 (2016).
29. El-Amine, M. et al. What explains the year-to-year variation in growing season timing of boreal black spruce forests? *Agr. For. Meteorol.* **324**, 109113 (2022).
30. Ren, Y. et al. Earlier spring greening in Northern Hemisphere terrestrial biomes enhanced net ecosystem productivity in summer. *Commun. Earth Environ.* **5**, 122 (2024).
31. Buermann, W. et al. Widespread seasonal compensation effects of spring warming on northern plant productivity. *Nature* **562**, 110–114 (2018).
32. Smith, N. E. et al. Spring enhancement and summer reduction in carbon uptake during the 2018 drought in northwestern Europe. *Philos. Trans. R. Soc. B* **375**, 20190509 (2020).
33. Peters, W. et al. Increased water-use efficiency and reduced CO_2 uptake by plants during droughts at a continental scale. *Nat. Geosci.* **11**, 744–748 (2018).
34. Lian, X. et al. Summer soil drying exacerbated by earlier spring greening of northern vegetation. *Sci. Adv.* **6**, eaax0255 (2020).
35. Yuan, W. P. et al. Redefinition and global estimation of basal ecosystem respiration rate. *Glob. Biogeochem. Cycles* **25**, GB4002 (2011).
36. Moyano, F. E., Manzoni, S. & Chenu, C. Responses of soil heterotrophic respiration to moisture availability: an exploration of processes and models. *Soil Biol. Biochem.* **59**, 72–85 (2013).
37. Curiel Yuste, J. et al. Microbial soil respiration and its dependency on carbon inputs, soil temperature and moisture. *Glob. Change Biol.* **13**, 2018–2035 (2007).
38. Niu, S. et al. Temperature responses of ecosystem respiration. *Nat. Rev. Earth Environ.* **5**, 559–571 (2024).
39. Canada's preliminary greenhouse gas emissions 1990–2023 (Environment and Climate Change Canada). *Goverment of Canada* https://www.canada.ca/ghg-inventory (2025).
40. Griffis, T. J. et al. Seasonal variation and partitioning of ecosystem respiration in a southern boreal aspen forest. *Agr. For. Meteorol.* **125**, 207–223 (2004).
41. Krishnan, P. et al. Impact of changing soil moisture distribution on net ecosystem productivity of a boreal aspen forest during and following drought. *Agr. For. Meteorol.* **139**, 208–223 (2006).
42. Beamesderfer, E. R., Arain, M. A., Khomik, M. & Brodeur, J. J. The impact of seasonal and annual climate variations on the carbon uptake capacity of a deciduous forest within the Great Lakes region of Canada. *J. Geophys. Res. Biogeosci.* **125**, e2019JG005389 (2020).
43. Crous, K. Y., Uddling, J. & De Kauwe, M. G. Temperature responses of photosynthesis and respiration in evergreen trees from boreal to tropical latitudes. *N. Phytol.* **234**, 353–374 (2022).
44. Alvarez, G. et al. Catalytic power of enzymes decreases with temperature: new insights for understanding soil C cycling and microbial ecology under warming. *Glob. Change Biol.* **24**, 4238–4250 (2018).
45. Boone, R. D., Nadelhoffer, K. J., Canary, J. D. & Kaye, J. P. Roots exert a strong influence on the temperature sensitivity of soil respiration. *Nature* **396**, 570–572 (1998).
46. Varney, R. M., Chadburn, S. E., Burke, E. J. & Cox, P. M. Evaluation of soil carbon simulation in CMIP6 Earth system models. *Biogeosciences* **19**, 4671–4704 (2022).
47. Arora, V. K. et al. Carbon–concentration and carbon–climate feedbacks in CMIP6 models and their comparison to CMIP5 models. *Biogeosciences* **17**, 4173–4222 (2020).
48. Ballantyne, A. et al. Accelerating net terrestrial carbon uptake during the warming hiatus due to reduced respiration. *Nat. Clim. Change* **7**, 148–152 (2017).
49. Yuan, X. et al. Weakening of global terrestrial carbon sequestration capacity under increasing intensity of warm extremes. *Nat. Ecol. Evol.* **9**, 124–133 (2025).
50. Xu, C. G. et al. Increasing impacts of extreme droughts on vegetation productivity under climate change. *Nat. Clim. Change* **9**, 948–953 (2019).

---

[1]Jiangsu Provincial Key Laboratory for Advanced Remote Sensing and Geographic Information Technology, International Institute for Earth System Science, Nanjing University, Nanjing, China. [2]Frontiers Science Center for Critical Earth Material Cycling, Nanjing University, Nanjing, China. [3]Jiangsu Center for Collaborative Innovation in Geographical Information Resource Development and Application, Nanjing, China. [4]Institute of Carbon Neutrality, Sino-French Institute for Earth System Science, College of Urban and Environmental Sciences, Peking University, Beijing, China. [5]Laboratoire des Sciences du Climat et de l'Environnement, LSCE/IPSL, CEA-CNRS-UVSQ, Université Paris-Saclay, Gif-sur-Yvette, France. [6]Environmental Sciences Group, Wageningen University, Wageningen, the Netherlands. [7]Jet Propulsion Laboratory, California Institute of Technology, Pasadena, CA, USA. [8]Department of Atmospheric and Oceanic Science, Earth System Interdisciplinary Center, University of Maryland, College Park, MD, USA. [9]State Key Laboratory of Tibetan Plateau Earth System, Environment and Resources, Institute of Tibetan Plateau Research, Chinese Academy of Sciences, Beijing, China. [10]Earth System Division, National Institute for Environmental Studies, Tsukuba, Japan. [11]Université de Montréal, Département de géographie, Montréal, Quebec, Canada. [12]School of Earth, Environment and Society and McMaster Centre for Climate Change, McMaster University, Hamilton, Ontario, Canada. [13]Global Institute for Water Security, University of Saskatchewan, Saskatoon, Saskatchewan, Canada. [14]Key Laboratory of Ecosystem Network Observation and Modeling, Institute of Geographic Sciences and Natural Resources Research, Chinese Academy of Sciences, Beijing, China. [15]College of Natural Resources and Environment, Northwest A&F University, Yangling, China. [16]Key Laboratory of Digital Earth Science, Aerospace Information Research Institute, Beijing, China. [17]Chongqing Jinfo Mountain Karst Ecosystem National Observation and Research Station, School of Geographical Sciences, Southwest University, Chongqing, China. [18]State Key Laboratory of Climate System Prediction and Risk Management, Jiangsu Collaborative Innovation Center of Atmospheric Environment and Equipment Technology, School of Environmental Science and Engineering, Nanjing University of Information Science & Technology, Nanjing, China. [19]Earth Systems Research Center, Institute for the Study of Earth, Oceans, and Space, University of New Hampshire, Durham, NH, USA. [20]School of Geography and Planning, Sun Yat-sen University, Guangzhou, China. [21]Faculty of Environment,

Science and Economy, University of Exeter, Exeter, UK. [22]Laboratoire de Météorologie Dynamique, Institut Pierre-Simon Laplace, CNRS, École Normale Supérieure, Université PSL, Sorbonne Université, École Polytechnique, Paris, France. [23]Hawkesbury Institute for the Environment, Western Sydney University, Penrith, New South Wales, Australia. [24]School of Life Sciences, Faculty of Science, University of Technology Sydney, Ultimo, New South Wales, Australia. [25]Canadian Centre for Climate Modelling and Analysis, Environment and Climate Change Canada, Victoria, British Columbia, Canada. [26]NSF National Center for Atmospheric Research, Climate and Global Dynamics, Boulder, CO, USA. [27]Department of Geographical Sciences, University of Maryland, College Park, MD, USA. [28]Oak Ridge National Laboratory, Environmental Sciences Division and Climate Change Science Institute, Oak Ridge, TN, USA. [29]Centre National de Recherches Météorologiques, Université de Toulouse, Météo-France, CNRS UMR, Toulouse, France. [30]Ludwig-Maximilians-Universität München, Munich, Germany. [31]Potsdam Institute for Climate Impact Research, member of the Leibniz Association, Potsdam, Germany. [32]Wyss Academy for Nature, University of Bern, Bern, Switzerland. [33]Climate and Environmental Physics, Physics Institute, University of Bern, Bern, Switzerland. [34]Oeschger Centre for Climate Change Research, University of Bern, Bern, Switzerland. [35]Max Planck Institute for Biogeochemistry, Jena, Germany. [36]Institute of Applied Energy, Tokyo, Japan. [37]Department of Geography and Planning, University of Toronto, Toronto, Ontario, Canada. [38]School of Geographical Sciences, Institute of Geography, Fujian Normal University, Fuzhou, China. ✉e-mail: jiangf@nju.edu.cn

Methods

GCB2024 atmospheric inversions

There are 14 atmospheric inversion models in the GCB2024 ensemble[1,51], in which 6 models assimilated satellite observations or both satellite and surface observations (that is, GCB2024-satellite) (Supplementary Table 3). The remaining eight inversions only assimilated surface CO_2 observations (that is, GCB2024-in-situ) (Supplementary Table 4). The GCB2024 inversions provide monthly NBP estimates at 1° × 1° spatial resolution. Due to the limited observational coverage of Canada in 2023 within the surface CO_2 dataset used (that is, ObsPack NRTv9.2, which includes Canadian data only up to February 2023), we focus primarily on the results based on the GCB2024-satellite inversions, including CMS-Flux[52], CAMS-Satellite[53,54], GONGGA[55,56], COLA[57], Global Carbon Assimilation System version 2 (GCASv2)[24] and NTFVAR[58,59]. For GCB2024 inversions, we calculate the mean across the ensembles as the optimal NBP estimates (sink positive/source negative) and the standard deviation as the uncertainty of NBP estimates (Supplementary Table 5).

GCASv2

At regional scales, the constraints provided by satellite observations may be insufficient, meaning that the choice of a priori fluxes can influence the inversion results[60]. Therefore, GCASv2 was used to conduct extra atmospheric inversion experiments (that is, GCAS-extra) with different wildfire emissions and prior NEP by assimilating the Orbiting Carbon Observatory 2 (OCO-2) XCO_2 observations[24]. GCASv2 integrates the Model for Ozone and Related Chemical Tracers version 4 (MOZART-4)[61] and the Ensemble Square Root Filter optimization (EnSRF)[62] to simulate atmospheric CO_2 concentrations and to produce the surface flux inversions, respectively. In this study, GCASv2 was run from September 2014 to January 2024 with a data assimilation (DA) window of 1 week. For each DA window, the system uses a two-step calculation method, that is, the prior fluxes are optimized using observations and then the optimized fluxes are put into MOZART-4 to simulate the initial atmospheric CO_2 fields for the next window. In addition, a 'super-observation' scheme is applied to reduce the representative error of observations by averaging all observations located in the same model grid and a single DA window. GCASv2 has been widely used in the estimates of global and regional carbon sinks[1,63]. More details about the description of GCASv2 can be found in ref. 24.

Ocean fluxes and fossil fuel emissions were obtained from the JMA Ocean CO_2 map[64] and GCP-GridFEDv2023.1[65], respectively; wildfire emissions were obtained from the Global Fire Emissions Databases v4.1 (GFED4.1s)[66] and the CAMS GFAS[67]; the prior biosphere fluxes were derived from the multiyear averaged NEP simulated by the BEPS model[68,69] (2013–2022) and the CASA-GFED4.1s model (2011–2020, obtained from CT2022[70]). By using the multiyear averages of prior fluxes in each year, we ensure the posterior NBP IAV are obtained exclusively through the constraints of satellite XCO_2 observations. Here, the bias-corrected OCO-2 XCO_2 retrievals (ACOS v11.1r L2 lite) were adopted[71], and both land (Land Nadir + Land Glint, LNLG) and ocean (Ocean Glint, OG) retrievals with XCO2_quality_flag = 0 were used for assimilation. A recent inversion experiment has shown that the inverted NBP over boreal North America cannot be affected by assimilating OG of OCO-2 XCO_2 retrievals[72]. The LNLG and OG XCO_2 retrievals were regridded to 1° × 1° and 5° × 5° spatial resolutions, respectively, and converted to the X2019 scale of the World Meteorological Organization[73].

Four inversion experiments with different prior fluxes were conducted: BEPS&GFED, BEPS&GFAS, CASA&GFED and CASA&GFAS. For each experiment, only terrestrial biosphere and ocean fluxes were optimized, while carbon emissions from fossil fuels and fires were prescribed[63,74]. The GCAS-extra inversions provide monthly NBP estimates at 1° × 1° spatial resolution. We utilize the mean value across the four experiments as the optimal NBP estimate and the standard deviation as its uncertainty for the GCAS-extra inversions (Supplementary Table 5).

Wildfire carbon emission estimates

Two datasets for wildfire carbon emissions were selected, including GFED4.1 s (0.25° × 0.25° and 3-h resolutions)[66] and GFAS (0.1° × 0.1° and daily resolutions)[67]. Both datasets provide carbon emissions for CO_2, carbon monoxide (CO) and methane (CH_4). Each emission data point was aggregated to 1° × 1° and monthly resolutions using the first-order conservative interpolation method from Climate Data Operators. In this study, the total wildfire carbon emissions ($\mathrm{Fire}_{\mathrm{total}}$) for each dataset were calculated by combining the emissions of CO_2, CO and CH_4:

$$\mathrm{Fire}_{\mathrm{total}} = \mathrm{Fire}_{\mathrm{CO_2}} + \mathrm{Fire}_{\mathrm{CO}} + \mathrm{Fire}_{\mathrm{CH_4}}, \tag{1}$$

where $\mathrm{Fire}_{\mathrm{CO_2}}$, $\mathrm{Fire}_{\mathrm{CO}}$ and $\mathrm{Fire}_{\mathrm{CH_4}}$ represent emissions of CO_2, CO and CH_4, respectively. The comparison between the 2023 Canadian wildfire carbon emissions calculated from GFED4.1s and GFAS and a recent top-down estimate using satellite CO observations (that is, Byrne wildfire emissions)[26] show that the mean of GFED4.1s and GFAS emissions (MGG) is closest to the Byrne emissions (Fig. 1a). Because Byrne et al.[26] reported Canadian wildfire emissions only for May–September 2023, and therefore they cannot be used to calculate 2023 anomalies relative to 2015–2022, we use the MGG dataset as the optimal wildfire emission estimates in this study.

NEP, GPP and TER estimates

In most GCB2024 inversion models (including GCASv2), wildfire emissions are either prescribed or ignored entirely. While some models (for example, NISMON-CO2) attempt to optimize NEP (sink positive/source negative) and wildfire emissions separately, atmospheric inversions cannot effectively distinguish their individual contributions to NBP. Consequently, overestimated wildfire emissions inevitably produce overestimated NEP estimates (and vice versa), regardless of whether wildfire adjustments are applied. Thus, only NBP estimates are reliable in atmospheric inversions. For this reason, NEP must be derived using equation (2) based on the optimized NBP from atmospheric inversions and optimal wildfire carbon emission estimates:

$$\mathrm{NEP} = \mathrm{NBP} + \mathrm{Fire}_{\mathrm{CO_2+CO\times14\%+CH_4\times14\%}}, \tag{2}$$

where NBP represents the NBP from the GCAS-extra and GCB2024 atmospheric inversions. It should be noted that, although the wildfire-emitted CO and CH_4 are ultimately converted into CO_2 though atmospheric chemical reactions, CO and CH_4 are gases with long chemical lifetimes, and it takes time for them to convert into CO_2. The NBP of the Canadian forests are mainly constrained by the satellite XCO_2 observations over Canada, which can only detect the part of CO and CH_4 that are transformed to CO_2 in the boundary layer of Canada. Based on atmospheric chemistry simulations in Europe, Ciais at al.[75] showed that only 14% of CO and CH_4 can be transformed to CO_2 in the boundary layer over the European continent. Considering that the area of Canada is comparable in size to Europe, this conversion factor (14%) was directly applied in this study to estimate the transformation of CO and CH_4. Therefore, in equation (2), $\mathrm{Fire}_{\mathrm{CO_2+CO\times14\%+CH_4\times14\%}}$ represents the total wildfire CO_2 emissions and 14% of CO and CH_4 emissions.

We assume a 20% uncertainty in wildfire emission estimates[22] (Supplementary Table 5). The uncertainty of NEP estimates was calculated as follows[22]:

$$\sigma_{\mathrm{NEP}} = \sqrt{\sigma^2_{\mathrm{NBP}} + \sigma^2_{\mathrm{Fire}_{\mathrm{CO_2+CO\times14\%+CH_4\times14\%}}}}, \tag{3}$$

where σ_{NBP} represents the uncertainties of NBP estimates. $\sigma_{\mathrm{Fire}_{\mathrm{CO_2+CO\times14\%+CH_4\times14\%}}}$ represents uncertainty of wildfire carbon emissions for CO_2 and 14% of CO + CH_4. In other words, $\sigma_{\mathrm{Fire}_{CO_2+CO\times14\%+CH_4\times14\%}}$ is 20% of these wildfire carbon emissions.

Two satellite-derived GPP products were selected: GOSIF (global, OCO-2-based SIF product) GPP[76] and FluxSat v2.2 GPP[77]. Both GPP products were generated on the basis of machine learning methods and have been validated by ground observations[76,78]. The GOSIF GPP was derived from the OCO-2 SIF product, providing 8-day GPP estimates at 0.05° spatial resolution. The FluxSat GPP was generated using FLUXNET2015 site GPP and MODIS Nadir Bidirectional Reflectance Distribution Function-Adjusted Reflectance, providing daily GPP data at 0.05° spatial resolution. We aggregate these GPP products to 1° spatial resolution. Following Liu et al.[22], we use the mean of GOSIF GPP and FluxSat GPP as the optimal estimate, and a bootstrapping technique to estimate the uncertainty of GPP. In the bootstrapping technique, we randomly generated 1,000 samples and calculated GPP uncertainty by using the standard deviation of the bootstrapped GPP ensembles[22].

TER was calculated as the residual among GPP, atmospheric inversion-derived NBP and wildfire emissions:

$$\mathrm{TER} = \mathrm{GPP} - \mathrm{NBP} - \mathrm{Fire}_{CO_2+CO\times14\%+CH_4\times14\%}. \tag{4}$$

The uncertainty of TER estimates was calculated as follows[22]:

$$\sigma_{\mathrm{TER}} = \sqrt{\sigma_{\mathrm{GPP}}^2 + \sigma_{\mathrm{NBP}}^2 + \sigma_{\mathrm{Fire}_{CO_2+CO\times14\%+CH_4\times14\%}}^2}, \tag{5}$$

where σ_{GPP} represents the GPP uncertainty.

As mentioned above, the uncertainty in wildfire emissions can affect the NEP and TER estimates. To investigate this impact, we further perform a sensitivity test by excluding all fluxes from pixels with wildfire emissions exceeding a threshold (λ, unit: gC m^{-2} yr^{-1}). Using different thresholds, we calculate the NEP and TER anomalies in the remaining areas. The wildfire emission thresholds λ were set as 2,000, 1,500, 1,000, 500 and 200 gC m^{-2} yr^{-1}.

Outputs of TRENDYv13 DGVMs

The results constructed from atmospheric inversions, wildfire emissions and independent satellite GPP products were compared with the outputs of 14 DGVMs from the TRENDYv13 project[1,25], including CABLE-POP, CLASSIC, CLM6.0, EDv3, ELM, IBIS, ISBA-CTRIP, JSBACH, LPJmL, LPX-Bern, OCNv2, ORCHIDEEv3, SDGVM and VISIT (Supplementary Table 6). We choose monthly outputs, including GPP, autotrophic respiration (Ra), heterotrophic respiration (Rh), air temperature and RZSM, from the TRENDYv13 S3 simulations during 2015–2023, which were run with all forcing data including time-varying atmospheric CO_2, land use change and climate change. The climate forcing data were derived from the CRU-JRA55 dataset. The atmospheric CO_2 forcing data were derived from CO_2 concentration observations from National Oceanic and Atmospheric Administration (NOAA) stations. The land use change data were provided from land use harmonization data for GCB2024 (LUH2-GCB2024). TER was calculated as the sum of Ra and Rh; NEP was calculated as the difference between GPP and TER; for temperature and RZSM, the TRENDY variables of 'tas' and 'mrso' were selected, respectively. To match the atmospheric inversions resolution, monthly outputs of the TRENDYv13 DGVMs were regridded to 1° × 1° spatial resolution, using the first-order conservative interpolation (for carbon fluxes) and bilinear interpolation (for environmental variables) methods from Climate Data Operators.

In situ CO_2 concentration and flux observations

The atmospheric CO_2 observations in Canada were obtained from Observation Package (ObsPack) Data Products in NOAA Global Monitoring Laboratory[79] (obspack_co2_1_GLOBALVIEWplus_v10.1_2024-11-13). We selected only the stations with complete data records from April to August 2023. Hence, eight stations were used for analysis (Supplementary Table 7), distributing the Canadian forests from northwest to southeast. Data from each station were processed using the Savitzky–Golay filtering method and then used to generate monthly CO_2 concentrations. The SA in CO_2 concentrations for each year was calculated as the difference in CO_2 concentrations between April and August.

The EC CO_2 fluxes in Canadian forests were collected from AmeriFlux (https://ameriflux.lbl.gov/) and BERMS (https://water.usask.ca/berms/) databases[42,80–83]. These EC fluxes were quality controlled, filtered, gap-filled and partitioned using established methods[84]. The gap-filling and partitioning methods may slightly vary depending on the network or of the individual sites or site principal investigator preferences. These sites are listed in Supplementary Table 8.

Other data

The Canadian forested regions were identified by using the ecoregion map from CT2022[70], which contains 19 ecosystem types. Pixels dominated by 'conifer forest', 'mixed forest', 'northern taiga', 'forest/field', 'conifer snowy/coastal' and 'wooded tundra' at 1° spatial resolution were selected and considered as forested regions. The climate map was derived from the Köppen–Geiger climate classification at 1° spatial resolution for the present-day (1991–2020) climate conditions[85].

Monthly kNDVI data were derived from the MODIS MOD13A3 V6.1 product[86], which provides monthly NDVI data at 1 km spatial resolution. We aggregate the NDVI to 1° spatial resolution and converted it to kNDVI according to equation (6)[87]:

$$\mathrm{kNDVI} = \tanh\left(\mathrm{NDVI}^2\right). \tag{6}$$

The SIF data were derived from TROPOspheric Monitoring Instrument (TROPOMI) near-infrared band measurements[88]. The monthly air temperature, precipitation, snowmelt, snow cover, snow depth and solar radiation were derived from the fifth generation of the land component of the ECMWF reanalysis (ERA5-Land) dataset[89]. The vapour pressure deficit was obtained from the TerraClimate dataset[90]. The monthly RZSM data were derived from the GLDAS[91] dataset. We additionally used the EAR5-Land[89] dataset to test the TER–RZSM relationships. Because ERA5-Land does not provide RZSM directly, it was calculated on the basis of the soil moisture in all layers above 100 cm depth weighted by the depth of each soil layer. These variables were aggregated to 1° spatial resolution using the area-weighted method.

Statistical analysis

Considering the nonlinear response of TER to hydrothermal conditions[92,93], a second-order polynomial model was used to fit the TER–air temperature and TER–RZSM response curves for summer and each month of summer. Meanwhile, generally, GPP linearly affects TER during the growing season over Canada's forests[94], and thus we use a linear model to fit the TER–GPP relationship. Statistical significance of the model fitting was calculated using the *F*-test. Moreover, we test the model performance using Akaike information criterion (AIC)[95]. The tests show that the second-order polynomial model outperforms the linear model in fitting the TER–air temperature and TER–RZSM relationships (that is, $\mathrm{AIC}_{\mathrm{polynomial}} < \mathrm{AIC}_{\mathrm{linear}}$) and vice versa in fitting the TER–GPP relationship (that is, $\mathrm{AIC}_{\mathrm{polynomial}} > \mathrm{AIC}_{\mathrm{linear}}$).

To further quantify the contributions of GPP and environmental (air temperature and RZSM) changes to TER anomalies for summer 2023 relative to 2015–2022, we conduct a statistical analysis to separate the environment- and GPP-driven TER anomalies. We normalize air temperature, RZSM and GPP during the summer period of 2015–2023 and then fit them to TER as follows:

$$\mathrm{TER} = a_1 \times {Z_T}^2 + a_2 \times Z_T + b_1 \times {Z_{\mathrm{RZSM}}}^2 + b_2 \times Z_{\mathrm{RZSM}} + c + d \times Z_{\mathrm{GPP}}, \tag{7}$$

where a_1, a_2, b_1, b_2, c and d are regression coefficients. TER was constructed from atmospheric inversions, wildfire emissions and satellite-derived GPP products. Z_T, Z_{RZSM} and Z_{GPP} are the z-score value of air temperature, RZSM and GPP, respectively. We calculate the time series of summer TER data without GPP effects ($\mathrm{TER}_{\mathrm{environmental}}$) as follows:

$$\mathrm{TER}_{\mathrm{environmental}} = a_1 \times {Z_T}^2 + a_2 \times Z_T + b_1 \times {Z_{\mathrm{RZSM}}}^2 + b_2 \times Z_{\mathrm{RZSM}} + c. \quad (8)$$

We then calculate the anomalies of TER and $\mathrm{TER}_{\mathrm{environmental}}$ for 2023. Therefore, the anomalies of $\mathrm{TER}_{\mathrm{environmental}}$ was considered as the absolute contributions of environmental changes to 2023 TER anomalies, and the difference between anomalies of TER and $\mathrm{TER}_{\mathrm{environmental}}$ in 2023 was considered as the absolute contribution of GPP changes.

Data availability

All data used in this study are publicly available. The inversions of GCASv2 are available via Dryad at https://doi.org/10.5061/dryad.83bk3jb1h (ref. 96). The inversions of GCB2024 are available at https://doi.org/11676/GpFcABoKcZMVnRUlLHRInhdM. The GOSIF GPP are available at https://globalecology.unh.edu/data/GOSIF-GPP.html. The FluxSat v2.2 GPP are available at https://daac.ornl.gov/VEGETATION/guides/FluxSat_GPP_FPAR.html. The GFED4.1s fire emissions are available at https://www.geo.vu.nl/~gwerf/GFED/GFED4/. The CAMS GFAS fire emissions can be downloaded at https://www.ecmwf.int/en/forecasts/dataset/global-fire-assimilation-system. The TRENDY data are available at https://mdosullivan.github.io/GCB. The atmospheric CO_2 concentration data were obtained from the NOAA Global Monitoring Laboratory at https://gml.noaa.gov/ccgg/obspack/data.php. The EC data can be downloaded at https://ameriflux.lbl.gov and https://water.usask.ca/berms. CT2022 data are available at https://gml.noaa.gov/ccgg/carbontracker/index.php. The TROPOMI SIF data are available at https://radiantearth.github.io/stac-browser/#/external/data-portal.s5p-pal.com/api/s5p-l2/collections/L2__SIF__. The MODIS NDVI and GLDAS RZSM are available via the Google Earth Engine (GEE) platform at https://developers.google.com/earth-engine/datasets/. The Köppen–Geiger climate classification map can be downloaded at https://www.gloh2o.org/koppen/. The air temperature, precipitation, snowmelt, snow cover, snow depth and solar radiation from ERA5-Land and vapour pressure deficit from TerraClimate are publicly available via the GEE platform at https://developers.google.com/earth-engine/datasets/.

Code availability

The MATLAB codes used in this study are available via GitHub at https://github.com/Guanyu-nju/Canadian_forest_carbon.git.

References

51. Luijkx, I. et al. *Global CO_2 Gridded Flux Fields from 14 Atmospheric Inversions in GCB2024* (ICOS Data Portal, 2024).
52. Liu, J. et al. Carbon Monitoring System Flux Net Biosphere Exchange 2020 (CMS-Flux NBE 2020). *Earth Syst. Sci. Data* **13**, 299–330 (2021).
53. Chevallier, F. et al. Inferring CO_2 sources and sinks from satellite observations: Method and application to TOVS data. *J. Geophys. Res. Atmos.* **110**, D24 (2005).
54. Remaud, M., Chevallier, F., Cozic, A., Lin, X. & Bousquet, P. On the impact of recent developments of the LMDz atmospheric general circulation model on the simulation of CO_2 transport. *Geosci. Model Dev.* **11**, 4489–4513 (2018).
55. Jin, Z. et al. Constraint of satellite CO_2 retrieval on the global carbon cycle from a Chinese atmospheric inversion system. *Sci. China Earth Sci.* **66**, 609–618 (2023).
56. Nassar, R. et al. Modeling global atmospheric CO_2 with improved emission inventories and CO_2 production from the oxidation of other carbon species. *Geosci. Model Dev.* **3**, 689–716 (2010).
57. Liu, Z. et al. Improving the joint estimation of CO_2 and surface carbon fluxes using a constrained ensemble Kalman filter in COLA (v1.0). *Geosci. Model Dev.* **15**, 5511–5528 (2022).
58. Nayagam, L. et al. A top-down estimation of subnational CO_2 budget using a global high-resolution inverse model with data from regional surface networks. *Environ. Res. Lett.* **19**, 014031 (2024).
59. Maksyutov, S. et al. Technical note: a high-resolution inverse modelling technique for estimating surface CO_2 fluxes based on the NIES-TM–FLEXPART coupled transport model and its adjoint. *Atmos. Chem. Phys.* **21**, 1245–1266 (2021).
60. Zhang, L. et al. Improved estimates of net ecosystem exchanges in mega-countries using GOSAT and OCO-2 observations. *Commun. Earth Environ.* **5**, 737 (2024).
61. Emmons, L. K. et al. Description and evaluation of the Model for Ozone and Related chemical Tracers, version 4 (MOZART-4). *Geoscientific Model Dev.* **3**, 43–67 (2010).
62. Whitaker, J. S. & Hamill, T. M. Ensemble data assimilation without perturbed observations. *Mon. Weather Rev.* **130**, 1913–1924 (2002).
63. Friedlingstein, P. et al. Global Carbon Budget 2023. *Earth Syst. Sci. Data* **15**, 5301–5369 (2023).
64. Iida, Y., Takatani, Y., Kojima, A. & Ishii, M. Global trends of ocean CO_2 sink and ocean acidification: an observation-based reconstruction of surface ocean inorganic carbon variables. *J. Oceanogr.* **77**, 323–358 (2021).
65. Jones, M. W. et al. Gridded fossil CO_2 emissions and related O_2 combustion consistent with national inventories 1959–2018. *Sci. Data* **8**, 2 (2021).
66. van der Werf, G. R. et al. Global fire emissions estimates during 1997–2016. *Earth Syst. Sci. Data* **9**, 697–720 (2017).
67. Kaiser, J. W. et al. Biomass burning emissions estimated with a global fire assimilation system based on observed fire radiative power. *Biogeosciences* **9**, 527–554 (2012).
68. Chen, J. M. et al. Vegetation structural change since 1981 significantly enhanced the terrestrial carbon sink. *Nat. Commun.* **10**, 4259 (2019).
69. Chen, J. M., Liu, J., Cihlar, J. & Goulden, M. L. Daily canopy photosynthesis model through temporal and spatial scaling for remote sensing applications. *Ecol. Model.* **124**, 99–119 (1999).
70. Jacobson, A. R. et al. *CarbonTracker CT2022* (NOAA Global Monitoring Laboratory, 2023).
71. O'Dell, C. W. et al. Improved retrievals of carbon dioxide from Orbiting Carbon Observatory-2 with the version 8 ACOS algorithm. *Atmos. Meas. Tech.* **11**, 6539–6576 (2018).
72. Wang, X. et al. The role of OCO-3 XCO_2 retrievals in estimating global terrestrial net ecosystem exchanges. *Atmos. Chem. Phys.* **25**, 867–880 (2025).
73. Hall, B. D. et al. Revision of the World Meteorological Organization Global Atmosphere Watch (WMO/GAW) CO_2 calibration scale. *Atmos. Meas. Tech.* **14**, 3015–3032 (2021).
74. He, W. et al. Improved constraints on the recent terrestrial carbon sink over China by assimilating OCO-2 XCO2 retrievals. *J. Geophys. Res. Atmos.* **128**, e2022JD037773 (2023).
75. Ciais, P. et al. The impact of lateral carbon fluxes on the European carbon balance. *Biogeosciences* **5**, 1259–1271 (2008).
76. Li, X. & Xiao, J. A global, 0.05-degree product of solar-induced chlorophyll fluorescence derived from OCO-2, MODIS, and reanalysis data. *Remote Sens.* **11**, 517 (2019).
77. Joiner, J. & Yoshida, Y. Global MODIS and FLUXNET-derived daily gross primary production, V2 (ORNL Distributed Active Archive Center, 2021).
78. Joiner, J. & Yoshida, Y. Satellite-based reflectances capture large fraction of variability in global gross primary production (GPP) at weekly time scales. *Agr. For. Meteorol.* **291**, 108092 (2020).

79. Schuldt, K. N. et al. *Multi-laboratory Compilation of Atmospheric Carbon Dioxide Data for the Period 1957–2023; obspack_co2_1_GLOBALVIEWplus_v10.1_2024-11-13* (NOAA Global Monitoring Laboratory, 2024).
80. Helbig, M. et al. Direct and indirect climate change effects on carbon dioxide fluxes in a thawing boreal forest–wetland landscape. *Glob. Change Biol.* **23**, 3231–3248 (2017).
81. Barr, A., Black, T. A. & McCaughey, H. in *Phenology of Ecosystem Processes* (ed. Asko Noormets) 3–34 (Springer, 2009).
82. Peichl, M., Brodeur, J. J., Khomik, M. & Arain, M. A. Biometric and eddy-covariance based estimates of carbon fluxes in an age-sequence of temperate pine forests. *Agr. For. Meteorol.* **150**, 952–965 (2010).
83. Graveline, V. et al. Surface-atmosphere energy exchanges and their effects on surface climate and atmospheric boundary layer characteristics in the forest-tundra ecotone in northwestern Canada. *Agr. For. Meteorol.* **350**, 109996 (2024).
84. Lasslop, G. et al. On the choice of the driving temperature for eddy-covariance carbon dioxide flux partitioning. *Biogeosciences* **9**, 5243–5259 (2012).
85. Beck, H. E. et al. Present and future Köppen–Geiger climate classification maps at 1-km resolution. *Sci. Data* **5**, 180214 (2018).
86. Didan, K. *MODIS/Terra Vegetation Indices Monthly L3 Global 1 km SIN Grid V061 [Dataset]* (NASA EOSDIS Land Processes Distributed Active Archive Center., 2021).
87. Camps-Valls, G. et al. A unified vegetation index for quantifying the terrestrial biosphere. *Sci. Adv.* **7**, eabc7447 (2021).
88. Köhler, P. et al. Global retrievals of solar-induced chlorophyll fluorescence with TROPOMI: first results and intersensor comparison to OCO-2. *Geophys. Res. Lett.* **45**, 456–410,463 (2018).
89. Hersbach, H. et al. *ERA5 Monthly Averaged Data on Single Levels from 1959 to Present* (Copernicus Climate Change Service Climate Data Store, 2019).
90. Abatzoglou, J. T., Dobrowski, S. Z., Parks, S. A. & Hegewisch, K. C. TerraClimate, a high-resolution global dataset of monthly climate and climatic water balance from 1958-2015. *Sci. Data* **5**, 170191 (2018).
91. Rodell, M. et al. The Global Land Data Assimilation System. *Bull. Am. Meteorol. Soc.* **85**, 381–394 (2004).
92. Chen, W. et al. Evidence for widespread thermal optimality of ecosystem respiration. *Nat. Ecol. Evol.* **7**, 1379–1387 (2023).
93. Niu, S. L. et al. Thermal optimality of net ecosystem exchange of carbon dioxide and underlying mechanisms. *N. Phytol.* **194**, 775–783 (2012).
94. Ryan, M. G., Lavigne, M. B. & Gower, S. T. Annual carbon cost of autotrophic respiration in boreal forest ecosystems in relation to species and climate. *J. Geophys. Res. Atmos.* **102**, 28871–28883 (1997).
95. Akaike, H. A new look at the statistical model identification. *IEEE Trans. Autom. Control* **19**, 716–723 (1974).
96. Jiang, F. Canada's extreme wildfires dominate the decline in global land carbon sinks in 2023. *Dryad* https://doi.org/10.5061/dryad.83bk3jb1h (2024).

Acknowledgements

This work is supported by the National Key R&D Program of China (grant no. 2023YFB3907404 to F.J.), the National Natural Science Foundation of China (grant nos. 42125105 to Yongguang Zhang and 42377102 to F.J.), the Jiangsu Provincial Science Fund for Distinguished Young Scholars (grant no. BK20231530 to F.J.), the German Federal Ministry of Education and Research (BMBF), project STEPSEC (grant no. 01LS2102A to T.N.), the Environment Research and Technology Development Fund (grant no. JPMEERF24S12206 to E.K.) and the NASA Early Career Investigator Program in Earth Science (grant no. 80NSSC24K1632 to L.M.). To generate the JSBACH TRENDYv13 data, resources of the Deutsches Klimarechenzentrum (DKRZ) granted by its Scientific Steering Committee (WLA) under project ID bm1241 were used. E3SM results for TRENDYv13 were supported as part of the Energy Exascale Earth System Model (E3SM) project, funded by the US Department of Energy, Office of Science, Office of Biological and Environmental Research Earth Systems Model Development Program area of Earth and Environmental System Modeling. We thank C. Rödenbeck at Max Planck Institute for Biogeochemistry, Y. Niwa at National Institute for Environmental Studies, Japan, L. Feng and P. Palmer at University of Edinburgh, A. Jacobson at the Cooperative Institute for Research in Environmental Sciences, D. Yang at Institute of Atmospheric Physics, Chinese Academy of Sciences, N. Chandra at Research Institute for Global Change, and P. Patra at Japan Agency for Marine-Earth Science and Technology for providing the GCB2024-in-situ inversions. The OCO-2 data are produced by the OCO project at the Jet Propulsion Laboratory, California Institute of Technology, and obtained from the data archive at the NASA Goddard Earth Science Data and Information Services Center. We acknowledge all atmospheric data providers to obspack_co2_1_GLOBALVIEWplus_v10.1_2024-11-13. We especially thank D. Worthy at Environment and Climate Change Canada for his/her great efforts on Canada's CO_2 observations and data sharing. We thank R. Staebler at Environment and Climate Change Canada, J. J. Brodeur at McMaster University, X. Zhang at Nanjing University and B. Johnson at University of Saskatchewan for help in processing the EC data. We thank A. P. Walker at Oak Ridge National Laboratory for his comments on an earlier version of the manuscript. We are also grateful to the High-Performance Computing Center (HPCC) of Nanjing University for conducting the GCAS-extra inversions on its blade cluster system.

Author contributions

F.J. and G.D. conceptualized and designed the study. F.J. and G.D. performed the analyses and wrote the paper, with review by all authors. I.T.L., W.P., P.C., J.L., F.C., S.P., X.T., N.Z. and S.M. provided the GCB2024 inversion results. S.S., P.F., M.O., J.K., V.A., D.K., L.M., P.E.T., R.S., T.N., J.H., Q.S., S.Z., P.P., E.K. and B.L. provided the DGVM results. O.S., M.A.A. and A.G.B. provided the EC data.

Competing interests

The authors declare no competing interests.

Additional information

Supplementary information The online version contains supplementary material available at https://doi.org/10.1038/s41561-025-01875-1.

Correspondence and requests for materials should be addressed to Fei Jiang.

Peer review information *Nature Geoscience* thanks Bassil El Masri and the other, anonymous, reviewer(s) for their contribution to the peer review of this work. Primary Handling Editors: Camilla Brunello, Carolina Ortiz Guerrero and Aliénor Lavergne in collaboration with the *Nature Geoscience* team.